Prescriptive formulation of Inorganic Membranes on Aqueous Surface

Ghim Wei Ho (elehgw@nus.edu.sg)
National University of Singapore https://orcid.org/0000-0003-1276-0165
Chen Zhang
Department of Electrical and Computer Engineering, National University of Singapore
Wanheng Lu
Department of Electrical and Computer Engineering, National University of Singapore
Yingfeng Xu
Department of Electrical and Computer Engineering, National University of Singapore
K. Y. Zeng
National University of Singapore

Physical Sciences - Article

Keywords:

Posted Date: June 15th, 2022

DOI: https://doi.org/10.21203/rs.3.rs-1695724/v1

Prescriptive formulation of Inorganic Membranes on Aqueous Surface

Chen Zhang[1], Wanheng Lu[1], Yingfeng Xu[1], Kaiyang Zeng[4], Ghim Wei Ho[1,2,3]*

[1]Department of Electrical and Computer Engineering, National University of Singapore, Singapore 117583, Singapore
[2]Department of Materials Science and Engineering, National University of Singapore, Singapore 117575, Singapore
[3]Institute of Materials Research and Engineering, A*STAR (Agency for Science, Technology and Research), Singapore 117602, Singapore
[4]Department of Mechanical Engineering, National University of Singapore, 117576, Singapore
*Correspondence to elehgw@nus.edu.sg

Freestanding functional inorganic membranes have piqued immense interest, as they may extend the notion of a selective barrier beyond matter flow to encompass energy and even information flows[1], potentially unlocking new possibilities in advanced separation[2], catalysis[3], sensors[4,5], memories[6], optical filtering[7] and ionic conductors[8,9]. However, limited by the brittle nature of most inorganic materials along with their few surface unsaturated linkages[10], inorganic membranes are far less ubiquitous than their organic counterparts, which may be easily obtained from diverse top-down moldings and/or bottom-up syntheses[11]. Up to now, only a few specific inorganic membranes were circuitously derived from the pre-deposited films by selective removal of the sacrificial substrates[4-6,8,9]. Here, we demonstrate a facile strategy to switch the nucleation preference in the aqueous system, resulting in a versatile synthesis of various ultrathin inorganic membranes on solution surface. Through a comprehensive understanding of the kinematic evolution of floating building units for membrane construction, the phase diagram based on geometrical connectivity, as well as the principle of customizing membrane thickness and porosity, are established, providing access to unusual membrane topologies with complex architectures. This universal synthetic methodology, pivotal to both scientific and industrial communities, will hasten the exploitation of new functional membranes for a variety of novel applications.

In principle, the membrane construction relies on two conditions, *i.e.*, to constrain the matter distribution in two dimensions and maintain their geometric continuity. This conception has inspired the emergence

of ultrathin polymeric membrane prepared through interfacial polymerization (IP)[12,13], particularly at the gas-liquid interface[14,15], where the dynamic crosslink locally occurs with the self-organized attraction of monomers from the bulk solution, thus endowing the flexibilities in kinetic controllability and subsequent membrane transfer. These advances enlighten us to analogously think about the possibility of creating reactive inorganic units confined to an aqueous surface and organizing their in-plane linkages, ultimately pursuing unequivocal methodology to fabricate a library of freestanding inorganic membranes.

In a typical aqueous system for producing inorganic materials, due to the lowest free energy barrier (Supplementary Fig. 1, details in Supplementary Information, 'Section S1.1'), solid nuclei formation on the vessel wall is preferred over that on the aqueous surface and homogeneous nucleation within the solution (Fig. 1a and 1b). Such undesired nucleation affinity, disclosed by probing the force indentation curve on the interface using underwater atomic force microscopy (AFM), originates from the van der Waals attraction of the liquid-solid interface on adjacent solids, and further trapping them in a well-defined potential well (Fig. 1c). In fact, regardless of the vessel materials, the interfacial potential well is extensively identified in common aqueous systems (Extended Data Fig. 1). This discovery motivates us to devise a solid-liquid interface shielding (SLIS) strategy to shift the nucleation preference to the liquid-air interface, by simply using a hydrogel coating to raise the energy barrier for nucleation on the vessel wall (Fig. 1b). In this study, partially-hydrolyzed poly(vinyl acetate) (PVAAc) was employed, which possesses alternating hydrophilic and hydrophobic areas (Supplementary Fig. 2), allowing its rapid swelling into a bulk hydrogel in the aqueous solution with an elastic filament layer facing the fluid (Supplementary Figs. 3 and 4). This hydrogel coat, as expected, universally eliminates the potential well on the water-vessel interface and creates an eternal repulsion to any approaching solid (Fig. 1c and Extended Data Fig. 1). A subsequent atomic pair distribution function (PDF) technique unveiled the mechanism for our proposed SLIS strategy, and its essence may be synoptically described by a simple equation. Any approaching solids will cause a decrease in the conformational entropy ($\Delta S < 0$) of the coated hydrogel system[16,17] (Fig. 1d). This produces a repulsive entropic force F (at temperature of T and resulting displacement of z) to inhibit their adhesion[18], which equivalently leads to an additional energy barrier ($\Delta G_{\mathrm{SLIS}} > 0$) on the liquid-solid interface from an energetic standpoint.

$$T\frac{\partial S}{\partial z} = F = -\frac{\partial G_{\mathrm{SLIS}}}{\partial z}$$

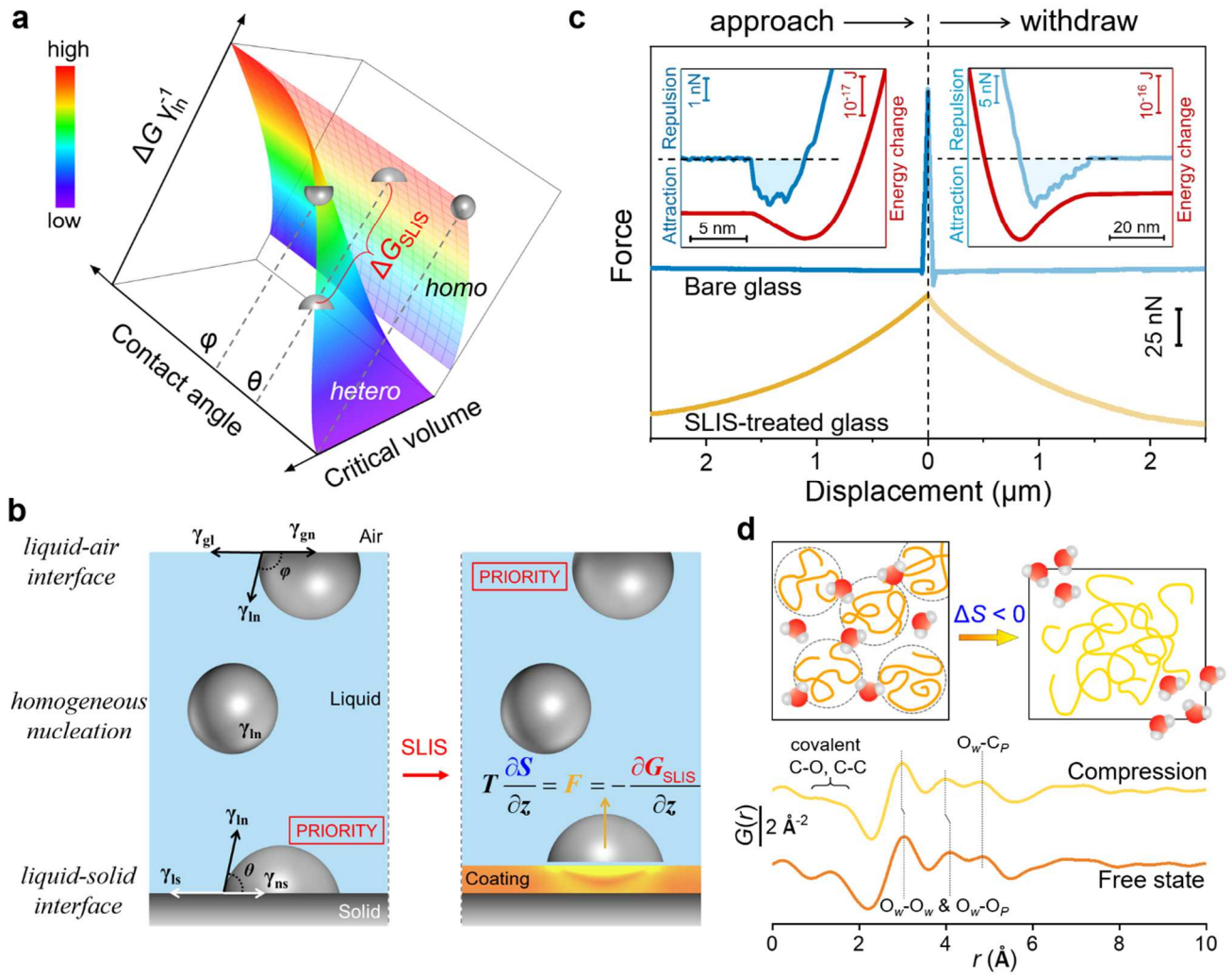

Figure 1. SLIS-induced conversion of the nucleation preference in aqueous solution. a, Sketch of the free energy change (ΔG) normalized to the interfacial tension between the liquid medium and the solid nucleus (γ_{ln}) through homogeneous nucleation (homo, upper meshed surface) and heterogeneous nucleation (hetero, bottom surface), as a function of the critical nucleus volume and the contact angle with the corresponding interface. The heterogeneous situation corresponds to two nucleation locations, namely the liquid-solid interface and liquid-air interface with the contact angle of θ and φ, respectively. **b**, Schematic illustration of three possible nucleation locations with the highlighted nucleation priority in a container-held solution system before and after SLIS treatment. **c**, AFM force-distance curves for the naked and SLIS-treated glass surfaces measured under water. The two insets zoom in the force-sensing regions and show the corresponding energy changes for the approach and withdraw process, respectively. For the naked glass, the sequential attraction and repulsion create a well-defined potential well on the liquid-glass interface for attracting and trapping the approaching solid from the liquid. This interfacial potential well is completely eliminated after SLIS treatment by producing the eternal interfacial repulsive force to the approaching solid. **d**, Microstructure diagrams and PDFs ($G(r)$) of the PVAAc hydrogel coating under free swelling and compressive load. The identified distances between 1.2 and 1.8 Å originate from the covalent C-O and C-C in PVAAc molecule. The two pair correlations at around 3 Å and 4 Å mainly belong to O-O distances from first and second neighbours, respectively.

Note that the O-O distance in the hydrogel system is resulted from a superimposed contribution from the relatively-short O_W-O_W (O in water molecule) and the relatively-long O_W-O_P (O in OH group of PVAAc network) distance. The pair correlation at about 4.8 Å belongs to O_W-C_P (C in PVAAc network) distance. The observed decrease in O-O distances when the hydrogel coating is compressed validates the lower proportion of O_W-O_P contribution, which is caused by the decreased density of hydrogen bonds between water and the PVAAc network. This confirms an enhancement in the structural order degree of the hybrid system comprised of PVAAc network and water molecules, namely the reduced entropy of mixing ($\Delta S < 0$), under a compressive loading.

We then chose the silver mirror reaction, a well-known aqueous process for producing solid deposit on the vessel surface[19], as a pilot practice of the proposed SLIS strategy. Strikingly, when this classic reaction was performed in the PVAAc-coated vessel, a piece of shiny Ag membrane was directly obtained on the solution surface (Fig. 2a), which can be easily suspended by a varnished wire ring (Fig. 2b). The conductivity mapping (Fig. 2c) indicates its structural homogeneity in morphology, density and thickness at the macro level. And the micro-level homogeneity was further confirmed by the scanning electron microscope (SEM, Fig. 2d and e, Supplementary Fig.5). Moreover, the freestanding Ag membrane, with just 189 nm in thickness, is of comparable Young's modulus (96.3 Gpa) to its polycrystalline bulk counterpart[20] (Fig. 2f and Supplementary Fig. 6). Meanwhile, the excellent flexibility is evidenced by the absence of fractures in these artificially-created wrinkles with a bending radius of several micrometers (Fig. 2d and Supplementary Fig. 7).

Beyond the initial success, the SLIS technique was further validated to be universal for the direct synthesis of various inorganic membranes on the solution surface, even for those materials that are conventionally inconceivable. As shown, the present membrane library involves forty-two elements in the periodic table (Fig. 2g and Extended Data Fig. 2a and b). Tremendous research efforts were expended to develop five representative membranes for each of the eight categories of classic materials (Supplementary Figs. 5-46), including elementary substances, oxides, sulfides, halides, hydroxides, metallates, nonmetallates and even coordination polymers, based on the three available types of aqueous reactions, *i.e.*, precipitation, hydrolysis and redox reaction. In terms of acting as functional mediators for various energy coupling and/or conversion (Extended Data Fig. 2c, Supplementary Tab. 2), these developed membranes promise an astounding diversity of unique applications. In addition, all the inorganic membranes can achieve several centimeters in dimension that is determined by the vessel size, and are uniform in thickness, ranging from tens of nanometers to several micrometers, thus endowing them the flexibility as opposed to their brittle bulk counterparts. Upon closer scrutiny, we found that

most of the membranes have irregular through-holes on their surfaces and some present crystallographic preferred orientation.

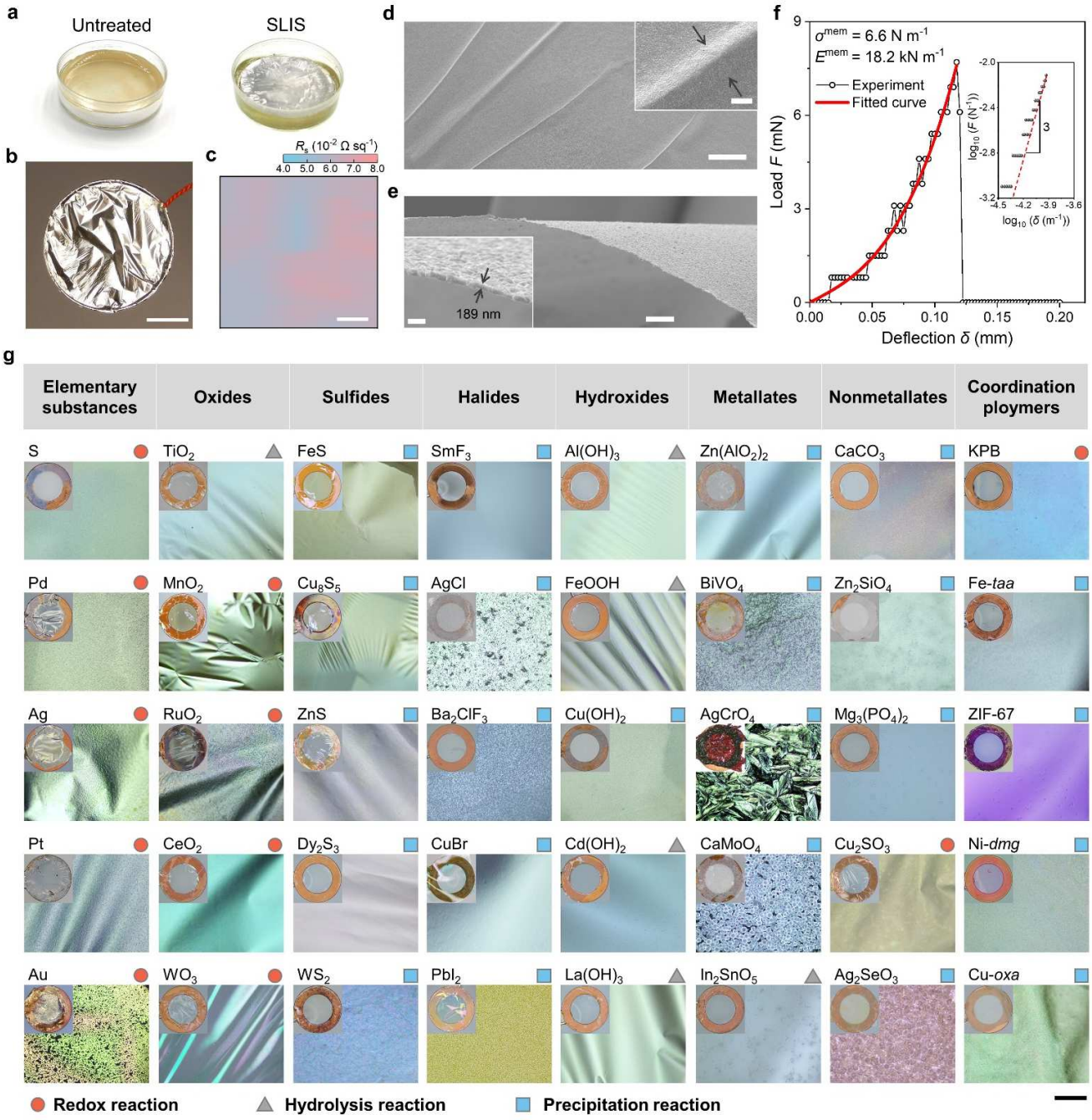

Figure 2. From pilot Ag membrane to unlocking a colourful membrane library. a, Digital photos of the completed silver mirror reaction performed in the untreated and SLIS-treated vessels. **b**, Image of the as-prepared Ag membrane suspended by a varnished wire ring. Scale bar, 1 cm. **c**, Sheet resistance mapping at 20 × 20 points on the Ag membrane with the test area of 10 × 10 mm^2. **d**, **e**, Top view (**d**) and side view (**e**) SEM images of the Ag membrane. The insets respectively zoom in a typical membrane wrinkle in (**d**) and the membrane edge in (**e**). **f**, Typical experimental loading curve of the through-hole Ag membrane and the curve fitting to the theoretical equation (Supplementary Fig. 6). The inset

highlights that the curve between load and deflection approaches cubic behavior at high loads. **g**, Optical microscope images of 40 freestanding membranes derived from the direct synthesis in the developed SLIS system, covering 8 categories of primary materials, i.e., elementary substances (S, Pd, Ag, Pt and Au), oxides (TiO_2, MnO_2, RuO_2, CeO_2 and WO_3), sulfides (FeS, Cu_8S_5, ZnS, Dy_2S_3 and WS_2), halides (SmF_3, AgCl, $BaClF_3$, CuBr and PdI_2), hydroxides (Al(OH), FeOOH, $Cu(OH)_2$, $Cd(OH)_2$ and $La(OH)_3$), metallates ($Zn(AlO_2)_2$, $BiVO_4$, Ag_2CrO_4, $CaMoO_4$ and In_2SnO_5), nonmetallates ($CaCO_3$, Zn_2SiO_4, $Mg_3(PO_4)_2$, Cu_2SO_3, and Ag_2SeO_3) and coordination polymers (KPB: K-containing prussian blue, Fe-*taa*: Fe(III)-polyphenol tannic acid complex, ZIF-67, Ni-*dmg*: Ni (II)-dimethylglyoxime complex and Cu-*oxa*: Cu(II)-oxalic acid complex). Note that the images were intentionally focused on the wrinkling membrane regions to highlight their flexible nature. The insets are the digital photos of the corresponding membranes suspended on a copper ring with a diameter of 4 mm. The mark at the top-right corner indicates the reaction types to prepare the membrane. Detailed characterizations of these as-prepared membranes are presented in Supplementary Figs. 5-46 and Tab. 1. Scale bars are 1 cm (**b**), 2 mm (**c**), 200 μm (**d**), 5 μm (**d** inset), 10 μm (**e**), 1 μm (**e** inset) and 200 μm (**g**).

Despite the effectiveness of SLIS strategy in supplying inorganic building blocks on the solution surface, their organization towards in-plane geometric continuity remains trial and error without understanding the general mechanism of membrane growth, which collaterally underpins the governance of a membrane's thickness and porosity. Accordingly, we developed a fast spectroscopic technique (see Supplementary Information, 'Section S3.1', Supplementary Figs. 47 and 48) to discern the reflection change of the aqueous surface throughout the Ag membrane formation (Fig. 3a), thus allowing us to identify all the critical developments during the structural evolution (Supplementary Fig. 49). The membrane growth is revealed to be governed by the kinematic of the floating building blocks in the SLIS-mediated system, with Brownian motion dominating the earlier stage and Cheerios effect, namely capillary attraction prevailing the mid-to-late phase (Fig. 3b). Once the reaction is initiated, numerous Ag particles with diameter of tens of nanometers are produced explosively on the aqueous surface (Fig. 3c). The formation of particles and their primary aggregation result in a drastic decrease in the interfacial reflectance due to their size-dependent surface plasmon resonance (SPR) absorption[21]. Through a developed AFM technique (Fig. 3d, Supplementary Fig. 50), these particles are found to float freely on the aqueous surface with in-plane Brownian motion. With continuous particle supply from the bulk solution, the occurrence of random collisions leads these isolated particles to stick together initially. As time goes on, the bigger particles featuring significantly reduced random mobility are formed[22], which are frequently collided and consequently grow into two-dimensional (2D) Brownian clusters (Fig. 3e). In theory, when the floating Brownian clusters grow adequately large, the guided Cheerios effect will

dominate, as the attractive capillary force between clusters overwhelms their random Brownian motion[23,24]. The interfacial indentation technique confirms the floating status of these Ag solid species on the aqueous surface with no water layer above (Extended Data Fig. 3, Supplementary Figs. 51 and 52), implying the inevitable Cheerios effect. Accordingly, these previously isolated Brownian clusters were discovered to readily link to adjacent clusters, as visually evidenced by their intensified cross-cell growth in the Voronoi mesh (Fig. 3e). Accompanied by progressively increasing optical reflectance, the ever-increasing aggregation of Brownian clusters/particles eventually leads to a critical state of (quasi)-bicontinuous network formation (Extended Data Fig. 4a-e). This denotes the least criterion in geometry to define a freestanding membrane. The transmission electron microscopy (TEM) analyses show the polycrystallinity and isotropic geometric permeability of this critical particle aggregate network (Extended Data Fig. 4f-j, see Supplementary Video 1), whose topology is revealed to be multifractal (Fig. 3f). These features imply a comprehensive impact of Brownian motion and Cheerios effect rather than a single dynamic mechanism. Moreover, through high-resolution TEM (HRTEM), plentiful twist boundaries are identified to be the physical junctions among the Ag particles (Fig. 3g, Extended Data Fig. 5, Supplementary Figs. 53 and 54). It confirms the instant welding of the Ag particles with active amorphous surface (Extended Data Fig. 5e and Supplementary Figs. 53c), ascribed to the capillary attraction-driven mechanical collision[25,26] (see Supplementary Information, 'Section S4.1', Supplementary Fig. 55). The collision energy is disclosed to be drastically intensified with the increasing size difference between the floating Brownian clusters under the action of capillary force (Fig. 3h). This theoretical foresight is in line with the experimental result that the subsequent evolution of the (quasi)-bicontinuous network can proceed smoothly with no kinetic obstruction. As more particles are captured by the solid branches, these meander-shaped vacant regions are progressively filled and evolve into well-defined closed holes. Thereafter, these holes gradually reduce in size along with the sharpening in the size distribution (Fig. 3i), till the holey membrane becomes compact.

One may doubt the universality of the as-indirectly-revealed kinematic process. The claims are corroborated by performing in-situ observation on other material systems involving the building units of various sizes and dimensions, namely discal AgCl, hemispherical $BiVO_4$ and claviform Ag_2CrO_4 particles. Regardless of the material categories, after an explosive formation of free particles floating on the aqueous surface, their critical (quasi)-bicontinuous networks are dynamically formed through the same procedure (see Supplementary Video 2, Supplementary Figs. 56-61). Essentially, it complies the

189 random Brownian motion-dominated initial particle assembly followed by collision-induced
190 connections among Brownian clusters accelerated by capillary attraction (Fig.3j, Supplementary Figs.
191 56, 58 and 60). Beyond these visual evidences, the quantization of the kinematic parameters verifies the
192 theoretical prediction (Supplementary Figs. 57, 59 and 61, Extended Data Fig. 6), that the smaller part
193 is considerably more vigorous than the opposite larger one in an attractive pair during the capillary
194 force-driven interattraction process. As a result, the network edge can extend epitaxially through the
195 efficient absorption of the fresh particles outside (Extended Data Fig. 7a-c, see Supplementary Video
196 3). Meanwhile, the interior these irregular holes are continuously separated into smaller but rounder
197 ones at the high-curvature sites by instant capturing of nascent particles within the network (Extended
198 Data Figs. 7d-e and 8, see Supplementary Information, 'Section S4.3', Supplementary Video 4). Such
199 a dynamic process provides the practical foundation to continuously adjust the membrane porosity by
200 simply controlling the evolution time.
201

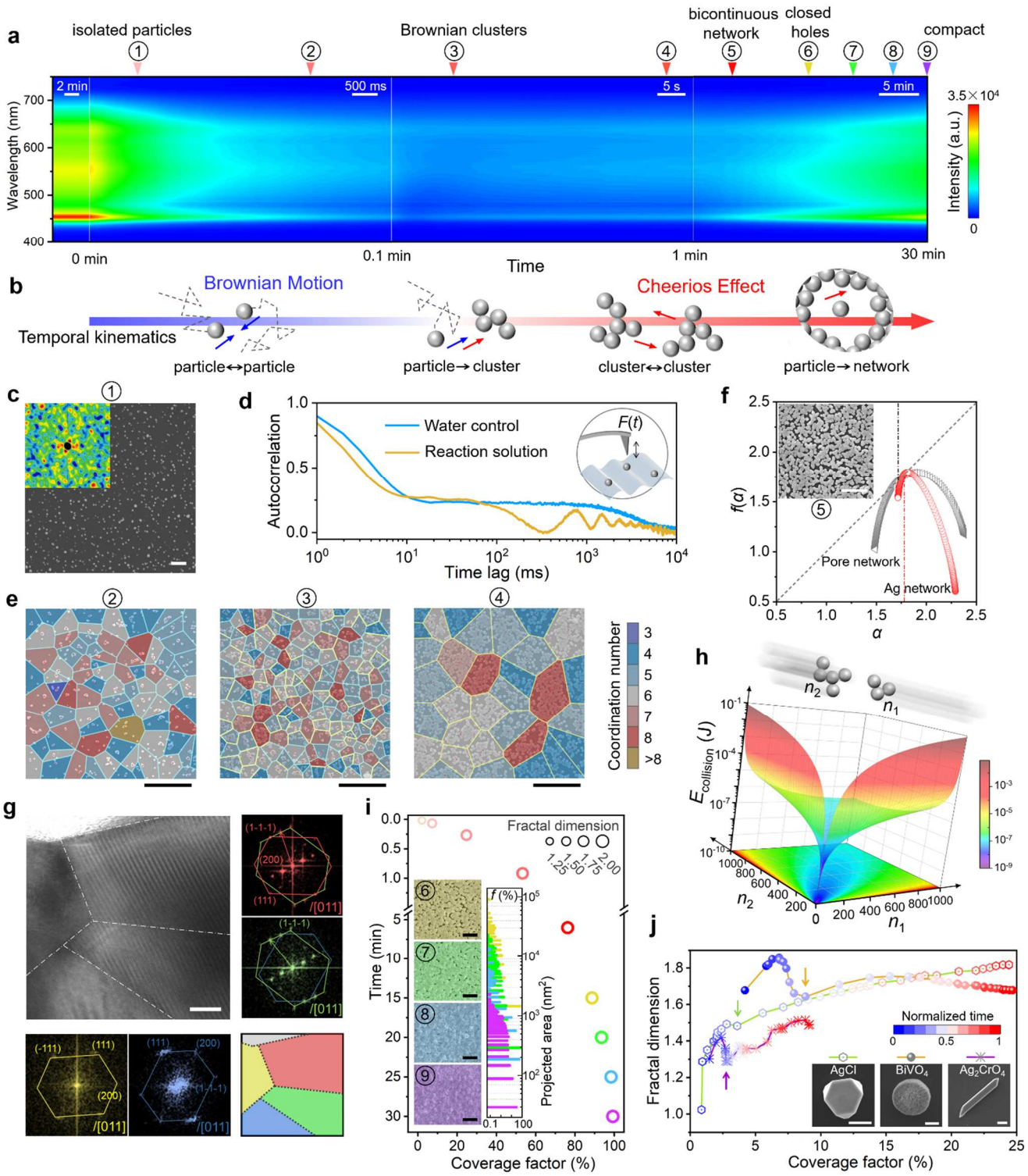

Figure 3. Kinematic-controlled membrane growth in SLIS system. a, Time-resolved reflectance spectra of the solution surface throughout the Ag membrane formation. The drastic variations in reflection, which is comprehensively resulted from the size-dependent SPR absorption of Ag particles and the linkage geometry-related specular reflection of Ag patches, help to identify the critical moments (indicated by the arrows and numbered above) associated with substantial changes in the status of floating silver solids. The corresponding characterizations can be recognized through the same numbered labels. **b**, Schematic diagram of the timeline showing the temporal kinematic of the block

units (particles or clusters) during membrane growth. **c**, Typical SEM image of the nascent floating Ag particles collected at 0.93 s after initiating the reaction. The inset shows the corresponding 2D autocorrelation analysis result confirming no spatial periodicity for the distribution of these particles. Scale bar, 1 μm. **d**, Autocorrelation analyses for the time series of the attraction between the aqueous surface and the suspended AFM tip as illustrated in the inset. In contrast to the case of blank water (blue line), the intensity fluctuation in the case of the reaction solution (yellow line) collected at 0.93 s indicates the floating Ag particles and their Brownian motion on the solution surface. **e**, Voronoi texture-meshed typical SEM images of the floating solid collected at 4.32, 17.1 and 53.5 s. The red dot indicates the center of each Brownian cluster. Colour of each cell denotes the coordination number as indicated in the right colour bar. Colour of the boundary highlights the connectivity between the adjacent cells, *i.e.*, blue denotes unconnected cells, and yellow denotes connected cells that are caused by the cross-domain growth of the Brownian cluster. **f**, Multifractal spectra of the solid Ag network and the complementary pore network in the typical SEM image of the (quasi)-bicontinuous Ag network collected at 6 min as shown in the inset. The auxiliary dashed lines help to identify the information dimension ($f(\alpha) = \alpha$). **g**, Typical HRTEM image of the (quasi)-bicontinuous Ag membrane containing plentiful nano-grains, which are connected by recognizable tilt and twist boundaries as indicated by the dashed lines. The bottom and right images are the corresponding fast Fourier transformed (FFT) images (bottom) and Fourier filtered images (right) of the marked regions, respectively. The dots in FFT images were labeled in the same colours as the corresponding interested regions indicated by the schematic at the bottom right corner. **h**, Calculated collision energy against the sizes of the two floating Brownian clusters driven by capillary attraction, which compose of n_1 and n_2 initial Ag particles, respectively. **i**, Time-course coverage factor and fractal dimension for the floating Ag membrane collected at 15, 20.5, 25.5 and 30 min. The inset shows their typical SEM images with pseudo colors and the projected area distribution of the through holes. **j**, Time-course coverage factors and fractal dimensions for the floating solids in the synthesis systems for AgCl, $BiVO_4$ and Ag_2CrO_4 membranes (see Supplementary Video 2). The time is recorded from the beginning of the reaction to the establishment of the critical (quasi)-bicontinuous network and normalized as indicated in the colour bar. The arrows highlight the moment corresponding to a drastic change in the time-course fractal dimension, when another kinetic mechanism starts to govern the network organization at the moment. The inset shows the typical SEM images of the corresponding building blocks, discal AgCl, hemispherical $BiVO_4$ and claviform Ag_2CrO_4 particles. Scale bars are 1 μm (**c**, **e**, **f** insert), 5 nm (**g**), 1 μm (**i** insets) and 5 μm (**j** insets).

The full understanding of membrane growth on aqueous surface encourages our further investigation into the criterion of membrane topologies formulation. Experimentally, after the reaction in bulk solution is completed, the floating Ag solids evolving from various initial reaction conditions present diverse patterns (Supplementary Fig. 62). These were simplified to construct a phase diagram based on graph theory[27,28] (GT, Fig. 4a), a mathematical method that focuses on the geometrical connectivity and organization complexity (Extended Data Tab. 1). Accordingly, we can identify four regimes depending on the reaction concentration and temperature, *i.e.*, node islands (*NI*), clique islands (*CI*), open network

(*ON*) and closed network (*CN*) in GT models. Both of the former two regimes with a low graph density and small complexity index, respectively corresponding to the isolated particles and Brownian clusters in practice, are non-membrane-forming phases. In the other two regimes, successful membrane formation and adjustable thickness across a three-order-of-magnitude range can be achieved. Nevertheless, the *CN* phase presents a higher complexity index and much smaller thickness compared to the *ON* phase.

Essentially, the kinematic difference during the organization of the floating building units causes the topological variance among the four GT phases. The fundamental steps of general membrane synthesis, including the random particle assembly into Brownian clusters and guided cluster aggregation into a continuous network, will face theoretical obstacles that represent the phase boundaries (see Supplementary Information, 'Section S6.1 and 6.2', Supplementary Figs. 63 and 64). Briefly, the floating particles maintain isolated and vigorous Brownian motion when they are tiny with low collision probability, thus forming a primitive *NI* phase. Only when this initial obstacle is surmounted (Fig. 4b), these tiny particles can organize into Brownian clusters. Similarly, the following barrier is whether the Cheerios effect-related capillary force among the particle clusters is strong enough to compete with their random Brownian motion (Fig. 4c). If not, these clusters will remain isolated, *i.e.*, in the *CI* phase. If it is, these clusters, with high kinetic energy from capillary force-driven acceleration, can mutually connect into a continuous network, forming the *CN* phase. Because the locomotor efficiency induced by capillary attraction is positively related to the size of floating species, whereas the Brownian motion has the reverse connection, there should be an extreme situation. When the initial building units is exceptionally enormous, they can bypass the Brownian motion stage and undergo direct connection driven by Cheerios effect, resulting in the *ON* phase with low graph density. These insights facilitate the kinematic simulation in achieving an intuitive understanding on the revealed four GT phases (See Supplementary Video 5).

From the disclosed kinematic criteria that are dependent on the size and density of the floating building units (Fig. 4b and c), we derive a qualitative phase diagram (Fig. 4d, Supplementary Fig. 65). This helps to predict membrane topologies from the perspective of reaction kinetics, thus underpinning a step-by-step guided synthesis approach for an unexplored inorganic membrane in the SLIS system (Extended Data Fig. 9). In general, for a targeted inorganic substance with the possibility to be produced in a mild aqueous reaction, the corresponding membrane synthesis can begin with an arbitrary initial

concentration and reaction temperature. By evaluating the structure of the floating solids after a sufficient time, one can assuredly adjust the reaction conditions of a new synthesis following the offered guidance. After a foolproof repetition of the prescribed experimental loop (Extended Data Fig. 9a), a well-defined membrane whose thickness and porosity can be customized by controlling the respective building unit size and reaction time, can be obtained.

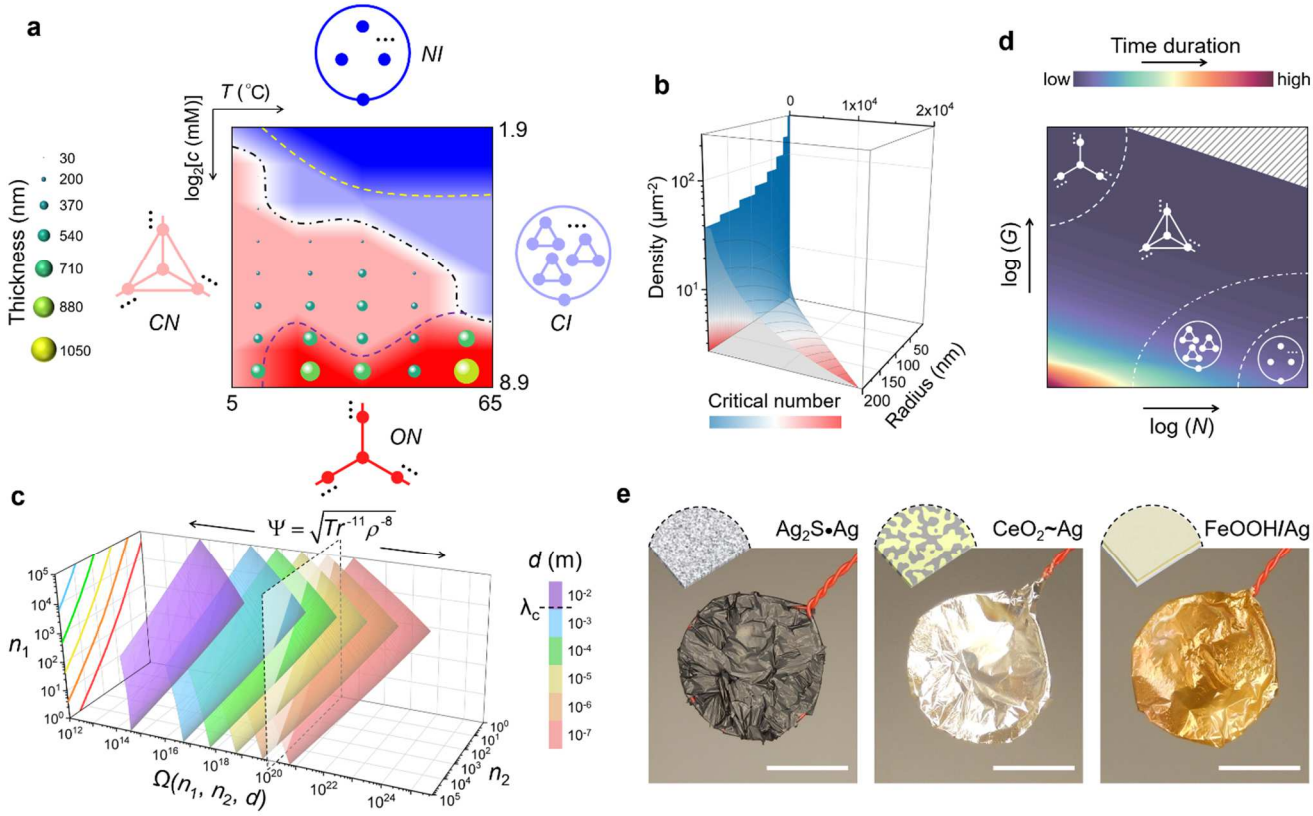

Figure 4. General synthetic methodology and extension of complexity for the SLIS-mediated membrane. a, Phase diagram based on the geometrical description of the patterned floating Ag solids evolving from different reaction temperatures T and initial concentrations of $[Ag(NH_3)_2]^+$ ($\log_2 c$). GT models for phases, including node islands (*NI*), clique islands (*CI*), open network (*ON*) and closed network (*CN*), are presented around in the same colour with that of the corresponding phase regime. Each bubble point in the phase diagram corresponds to the membrane thickness related to local T and $\log_2 c$ values, as indicated in the left colour bar. **b**, Criterion for the formation of the Brownian clusters with specific size depending on the particle radius and density. The coloured surface denotes the smallest number of particles in a Brownian cluster that may expand without encountering a kinetic barrier. **c**, Criterion for the aggregation of two Brownian clusters/particles in the phase space spanned by their size n_1, n_2 and initial distance d. The family of curved surface Ω is determined by n_1, n_2 and various d as indicated in the colour bar, whereas the reaction temperature T, the building unit's radius r and density ρ dictate the position of the mobilizable dashed plane Ψ. The region of $\Omega \geq \Psi$ represents the unimpeded

aggregation of two Brownian clusters/particles. These intersecting lines of surface family Ω and plane Ψ, that predict the critical n_1 and n_2 for varied cases of initial distance, are projected to the left plane with the same colour as the corresponding surface. Note that when the initial distance is larger than the capillary length of water λ_c (around 2.7 mm at room temperature), the determined curved surface will not intersect with the plane Ψ at any practical parameters. **d**, Phase diagram based on the density *N* and radial growth velocity *G* of the floating building units. Shadow region at top-right corner is not available due to the practical constraint of finite reactant supply. The colour bar indicates the time duration of running out of the feedstocks. **e**, Digital photos of three hybrid membranes derived from simple Ag membrane, including Ag_2S•Ag mixed membrane, CeO_2~Ag bicontinuous membrane and FeOOH/Ag stacked membrane, whose structures are illustrated in the top-left schematics, respectively. Scale bars, 1 cm.

In hindsight, the SLIS-mediated aqueous surface resembles a realistic 2D cellular automata[29,30]. As the reaction progresses with a given initial configuration, these chaotic floating seeds evolve into various delicate and tangible structures spontaneously. The comprehensive exploration of the kinematic rules provides a general synthetic methodology that drastically increases the kinds of available inorganic membranes, as well as a profound understanding of the dynamic emergence of complexity. Beyond the presented membrane library that has encompassed a wide range of functions (Extended Data Fig. 2c), complex membranes with topological diversity can be derived from simplex ones through further chemical conversion and physical integration (Fig. 4c, Supplementary Figs. 66-68), unlocking a unique dimension to the 2D world of membranes.

Methods

Materials and Reagents. Partially acetylated poly(vinyl alcohol) (poly(vinyl alcohol-co-vinyl acetate), PVAAc, 1750 ± 50, ≥ 99.0 %) was purchased from Sinopharm Chemical Reagent Co., Ltd., China. Anhydrous D(+)-glucose ($C_6H_{12}O_6$, ≥ 99.5 %), ammonium hydroxide (NH_3•H_2O, 28-30 %), phosphoric acid (H_3PO_4, ⩾85 wt%), sodium hydroxide (NaOH, ≥ 98.0 %), ammonium fluoride (NH_4F, ⩾ 99.99 %), titanium (IV) fluoride (TiF_4), aluminum chloride ($AlCl_3$, 99.99 %), calcium chloride ($CaCl_2$, ⩾ 99.9 %), manganese (II) chloride hydrate ($MnCl_2$•$4H_2O$, ≥ 98.0 %), iron (III) chloride ($FeCl_3$, 97 %), nickel (II) chloride ($NiCl_2$, 98 %), copper (II) chloride ($CuCl_2$, 99 %), cadmium chloride ($CdCl_2$, 99.99 %), barium chloride ($BaCl_2$, 99.9 %), copper (I) bromide (CuBr, ⩾ 98.0 %), sodium iodide (NaI, ⩾99.5 %), gold (III) chloride trihydrate ($HAuCl_3$•$3H_2O$, ≥ 99.9 %), ruthenium(III) chloride ($RuCl_3$), palladium (II) chloride ($PdCl_2$, ⩾ 99.9 %), chloroplatinic acid hydrate (H_2PtCl_6•xH_2O, ⩾ 99.9 %), potassium hexacyanoferrate (III) ($K_3Fe(CN)_6$, ⩾ 99.0 %), ammonium iron (III) citrate ($(NH_3)_xFe_yC_6H_8O_7$), cobalt (II) acetate tetrahydrate ($Co(CH_3COO)_2$•$4H_2O$, ⩾99 %), manganese (II)

acetate tetrahydrate ($Mn(CH_3COO)_2•4H_2O$, ≥ 99 %), sodium aluminate ($NaAlO_2$), ammonium metavanadate (NH_4VO_3, ≥ 99.0 %), potassium chromate (K_2CrO_4,≥ 99.0 %), sodium molybdate (Na_2MoO_4, ≥ 98 %), ammonium tetrathiotungstate ($(NH_4)_2WS_4$, ≥ 99.9%), potassium hydrogen carbonate ($KHCO_3$, 99.7 %), sodium metasilicate pentahydrate ($Na_2SiO_3•5H_2O$, ≥ 95.0 %), sodium sulfite (Na_2SO_3, ≥ 98.0 %), sodium thiosulfate pentahydrate ($Na_2S_2O_3 • 5H_2O$, ≥ 99.5 %), ammonium persulfate ($(NH_4)_2S_2O_8$, ≥ 98.0 %), zinc sulfate heptahydrate ($ZnSO_4•7H_2O$, ≥ 99.0 %), copper(II) sulfate pentahydrate ($CuSO_4 • 5H_2O$, ≥ 98.0 %), iron (II) sulfate heptahydrate ($FeSO_4•7H_2O$, ≥ 99.0 %), sodium phosphate tribasic dodecahydrate ($Na_3PO_4•12H_2O$, ≥ 98 %), magnesium nitrate hexahydrate ($Mg(NO_3)_2•6H_2O$, 99 %), silver nitrate ($AgNO_3$, ≥ 99.0 %), lanthanum (III) nitrate hexahydrate ($La(NO_3)_3•6H_2O$, 99.99 %), cerium (III) nitrate hexahydrate ($Ce(NO_3)_3•6H_2O$, 99.99 %), dysprosium(III) nitrate hydrate ($Dy(NO_3)_3 • xH_2O$, 99.9 %), samarium (III) nitrate hexahydrate ($Sm(NO_3)_3•6H_2O$, 99.9 %), lead (II) nitrate ($Pb(NO_3)_2$, ≥ 99.0 %), bismuth (III) nitrate pentahydrate ($Bi(NO_3)_3•5H_2O$, ≥ 98.0 %), tungsten powder (W, 99.95 %), sodium hypochlorite solution (NaClO, available chlorine 4.00-4.99 %), hypophosphorous acid solution (H_3PO_2, 50 wt% in H_2O), hydrazine hydrate ($N_2H_4•xH_2O$, 50-60 %), L-ascorbic acid ($C_6H_8O_6$, ≥ 99.0 %), tannic acid ($C_{76}H_{52}O_{46}$), oleamide ($C_{18}H_{35}NO$, ≥ 99 %), hexamethylenetetramine ($C_6H_{12}N_4$, ≥ 99.0 %), 2-methylimidazole ($CH_3C_3H_2N_2H$, 99 %), dimethylglyoxime ($CH_3C(=NOH)C(=NOH)CH_3$, ≥ 99.0 %) were purchased from Sigma-Aldrich Inc.. Hydrogen peroxide solution (H_2O_2, 30-32%) was purchased from QREC Chemical Co., Ltd. Hydrochloric acid (HCl, 37 %), sulfuric acid (H_2SO_4, 98 %) and nitric acid (HNO_3, 67-70 %) were purchased from Thermo Fisher Scientific Inc. Deionized water used was prepared from a TKA water purification system (Smart Pure 2).

Pretreatment on the reaction vessel. Without loss of generality, the consumable polystyrene Petri dish (Thermo Scientific, Φ35 × 10 mm) was employed as the reaction vessel for membrane synthesis. The inwall of the Petri dish was manually coated with the PVAAc film of about $1.6×10^{-2}$ mg mm^{-2}, which can rapidly swell into a hydrogel coat once it contacts with the aqueous solution. Briefly, the Petri dish was waggled sufficiently following the addition of 500 μL of PVAAc aqueous solution (3.5 wt%) to guarantee that all of its inwall surface was wetted by the solution. The pretreated Petri dish with PVAAc film coat was then obtained through desiccating it at 70 °C for 2 h, followed by naturally cooling down to the room temperature.

Membrane preparation. Detailed reactions and procedures for various membrane syntheses in the SLIS system were all involved in Supplementary Information (Section S2).

Membrane transfer, suspend and cut. To separate the floating membrane from the reaction Petri dish, the solution was firstly removed using a pipette followed by adding 8 mL DI water to re-float the membrane. The water inside the dish was further replaced for three times to fully eliminate residual chemicals. The membrane-held dish was then gently immersed in a large tank (usually a glass container with a diameter of 12 cm and a height of 6 cm) full with DI water, enabling the transfer of the cleaned membrane to a wider aqueous surface. To cut the membrane into the desired dimension, it was lifted by a hydrophobic acrylic plate, quickly cut with a razor blade before the water completely evaporated, and then released to re-float on the water surface for subsequent transfer. Regardless of substrate composition or surface topology, these water-floating membranes can be conveniently transferred to or suspended by a wide range of substrates, including silicon slice, acrylic plate, glass slide, copper ring,

varnished wire ring and conductive carbon tape in facing different characterizations. To adapt to the membranes with varied degrees of hydrophobicity and then prepare the flat membrane for XRD characterization, an optional hydrophilic surface of the hydrophobic acrylic plate was created by exposing it to 254 nm-UV light (NOVASCAN PSD-UVT) at room temperature for 15 min. Instead of DI water, the acetone solution (2~10 vol% in DI water) was used to clean and float those membranes that were not water resistant.

Structure characterizations. SEM images were acquired on a JEOL JSM-7001F with 15-kV electron beam equipped with a tiltable specimen stage. EDS data were collected using an Oxford X-max 50 detector. One side of the small piece of freestanding membranes was fixed on the conductive carbon tape for cross-sectional SEM observation. For EDS analysis, the membrane was transferred onto a flat silicon slice, copper foil or conductive carbon tape according to its chemical composition. TEM images were obtained on a JEM-2100F with 200-kV electron beam and the conductive Ag membrane was directly supported on a bare copper grid. FFT image processing was performed on DigitalMicrograph. The topography image of the membrane that supported by a flat silicon slice was obtained on a Bruker JPK NanoWizard Sense AFM equipped with a AC240-PP tip (OPUS, nominal spring force constant of 2 N m^{-1}). The corresponding thickness measurement was performed on the JPKSPAM data processing software. XRD patterns of membranes at room temperature were collected on a Bruker D8 ADVANCE at Cu K_α radiation (λ = 1.54056 Å) at a scanning rate of 4 ° min^{-1} with the X-ray tube voltage of 40 kV and current of 25 mA . The preferred orientation of the membrane was identified by completely indexing the XRD pattern, calculating each of the enhancements in the relative intensities compared to the polycrystalline standard pattern after removing the background, and recognizing the (*h k l*) value that corresponds to maximum enhancement. FTIR spectra were measured on a IRPrestige-21 spectrophotometer by using a Quest single-reflection ATR accessory equipped with a standard diamond puck.

Optical, electrical and wettability characterizations. Diffuse reflectance UV-Vis-NIR spectrum was obtained on a Shimadzu UV 3600 spectrophotometer with the wavelength range of 250 to 2500 nm. Room-temperature sheet resistance of Ag membrane was measured using a Keithley 2602 sourcemeter equipped with a M3TC four-point probe (4PP) and a Zolix TSM13-1 X-Y mobile station. The sheet resistance mapping was obtained by performing the measurements over an area of 10 × 10 mm^2 following a square 20 × 20 grid. Surface wettability test was performed at room temperature by placing 5 μL of sessile DI water droplet on the substrate surface. Based on the side-view picture shot by an H1600 industrial camera equipped with the S-EYE software, the relevant contact angle was determined using a specific plugin in ImageJ.

Optical observation of freestanding membranes. After a small piece of membrane with appropriate size (3 mm < dimension in each direction < 4 mm) was cut from a whole one, it was released to re-float onto DI water surface, then suspended over a copper ring with outer and inner diameters of 4 mm and 2 mm to ensure a single-layer membrane. The through-hole membrane was employed for optical observation on an Olympus BX53 microscope after a natural drying at room temperature.

Mechanics of the as-prepared freestanding Ag membrane. One face of the laser-cut PMMA ring (outer diameter Φ = 11mm, internal diameter 2*R* = 5 mm and thickness *h* = 3 mm, Supplementary Fig.

6) was firstly painted a thin PDMS coat (mixture of PDMS base and curing reagent in 10:1 ratio), followed by curing at 80 °C for 2 h. The coated side of the ring was then used to lift a water-floating Ag membrane with the dimension of 12 × 12 mm, which was subsequently dried at 50 °C for 30 min. The indentation measurement was performed at the center point of the membrane on a multitest 1-i tensile and compression test system (Mecmesin) by using a quartz rod (diameter Φ = 1 mm) with a hemispherical head. Before the measurement, the static electricity on the PMMA ring-suspended membrane and the quartz rod were fully eliminated by using Milty Zerostat 3. The loading rate was 1 mm min^{-1}. The relation between the force F and the indentation depth δ is given by[31-33]

$$\boldsymbol{F} = \sigma^{\mathrm{mem}} \pi \boldsymbol{R} \left(\frac{\delta}{\boldsymbol{R}} \right) + \boldsymbol{E}^{\mathrm{mem}} \boldsymbol{q}^3 \boldsymbol{R} \left(\frac{\delta}{\boldsymbol{R}} \right)^3$$

$$\boldsymbol{q} = 1.05 \; - \; 0.15\nu \; - \; 0.16\nu^2$$

where R is the radius of the Ag membrane, E^{mem} is the membrane Young's modulus and defined as $E^{\mathrm{mem}} = Et$, with the Young's modulus E and the membrane thickness t. σ^{mem} is the pretension and defined as $\sigma^{\mathrm{mem}} = \sigma t$, with the residual stress σ. q is a dimensionless constant that related the Poisson's ratio ν of silver (taken here as 0.37)[34]. The values of E^{mem} and σ^{mem} are obtained through curve fitting to the equation.

In-situ reflectance spectra during Ag membrane formation. The acquisition of in-situ reflectance spectra was carried out in a customized optical system as illustrated in Supplementary Fig. 47. To exclude ambient light, the measurements were performed in a sealed cuboid box (160×100×70 mm^3) with all faces painted black. After a pretrearted dish containing 1.5 mL of fresh Tollens' reagent solution (120 mM) was placed inside in the central position, an incident light beam (visible fiber-coupled UHP-T-LED, Prizmatix) with a collimator of 12 mm in diameter was fixed at 30 mm over the solution surface, and set at 90-degree angle from an opposite fiber detector of the spectrometer (Maya2000, Ocean Optics). To trigger the reaction, 1.5 mL of mixed D(+)-glucose (250 mM) and NaOH (50 mM) solution pre-stored in the dropper hanging over was instantly introduced into the system, and the in-situ reflectance spectra of the liquid-air interface were consecutively collected through SpectraSuite. The spectra in five minutes before triggering the reaction were collected at a rate of 0.2 Hz to estimate the stability of this customized measurement. The acquisition rates were set at 166.7 Hz, 20 Hz and 0.033 Hz respectively for the first 6 s, 6 to 60 s and the rest 29 min when the reaction was ignited. Critical time nodes were determined by mathematically identifying these moments containing extreme point of the recorded reflection intensity, which is a binary function of time and wavelength.

Brownian motion of the floating silver particles. To determine if the floating silver particles on the bulk solution surface have been exposed to the gaseous phase or are still completely immersed under the liquid-air interface, we developed an indirect technique based on the collection and analysis of the localized force signal on an Asylum MFP-3D system equipped with PPP-CONTPt-50 probe (NANOSENSORS, nominal spring force constant 0.2 N m^{-1}). As shown in the Supplementary Fig. 50a-c, the probe was suspended over the solution with a constant amplitude where the attraction between the water surface and the probe can be well-detected but out of the jump-to-contact distance. In addition to the intrinsic noise caused by the fluctuations of water surface, once any floating solid passed through the space between the solution surface and the probe, it would instantly diminish the attracting force

that the probe measured. Such additional disturbance $D(t)$ would be well-contained in the collected time series of force F(t) (converted from the amplitude signal) and significantly influence its autocorrelation result. At interested time node of 1 s after initiating the silver mirror reaction in the SLIS system, the reaction was terminated by immediately replacing the reaction solution by equivoluminal DI water. Beside the DI water as a blank control, the aforementioned approach was performed to these particle/solution systems for 100 s with the collection frequency of 1024 Hz. The subsequent autocorrelation analysis of the time series $F(t)$ was performed by using the Matlab built-in autocorrelation function (ACF) according to the follows:

$$\boldsymbol{ACF}(\tau) = \sum_{t=\tau+1}^{n} \frac{(\boldsymbol{F}_{(t)} - \bar{\mathrm{F}})(\boldsymbol{F}_{(t+\tau)} - \bar{\mathrm{F}})}{\sum_{t=1}^{n} (\boldsymbol{F}_{(t)} - \bar{\mathrm{F}})^2}$$

where $\bar{\mathrm{F}}$ is the mean value of the collected time series and τ is the time lag. There is significant difference between the autocorrelation results for the cases of blank water surface and the particles-floated solution surface (Supplementary Fig. 50d-f). The latter case presents oscillatory autocorrelation peaks at different time scales, which were further confirmed to be an intrinsic signal feature instead of originating from noise. These oscillatory autocorrelation peaks are derived from the modulation effect on the detected force by the probe when these air-exposed particles pass through the space between the solution surface and the probe. Evidently, these results confirm that these silver particles generating from the bulk solution have passed through the liquid-air interface and exposed to the air. In addition, these floating particles keep in random 2D Brownian motion on the aqueous surface.

AFM measurements. AFM force-distance curves obtained from the indentation experiments were conducted on an Asylum MFP-3D scanning probe microscopy system equipped with a PPP-CONTPt-50 probe (NANOSENSORS, nominal spring force constant of 0.2 N m^{-1}). The actual spring force constants in different situations were calibrated by acquiring force-distance curves on a stiff glass surface. To obtain the coated substrate, 10 μL of PVAAc aqueous solution (3.5 wt%) was applied thoroughly onto the surface of the bare substrate (1×1 cm^2 in area) at 70 °C in an oven, then desiccated for 2 h. To measure the surface mechanical properties of various substrates in aqueous system, the substrate was fixed at the bottom of a Petri dish (37×7 mm) and followed by adding 3 mL of DI water of room temperature to immerse it. The probe was then completely submerged to perform measurement after the water level was stabilized. All the force curves were recorded under the same loading and unloading rate of 1.5 μm s^{-1}. The displacement (x)-dependent potential energy change (ΔE) between x_0 and x_1 was obtained by using the recorded force curve $F(x)$ according to the following equation:

$$\Delta \boldsymbol{E} = -\int_{x_0}^{x_1} \boldsymbol{F}(\boldsymbol{x}) \boldsymbol{dx}$$

Force maps of the interested interfaces, including the control air-DI water interface and the interface between air and the on-site floating Ag membrane (30 min after igniting the silver mirror reaction in SLIS system), were performed over an area of 10×10 μm^2 following a square 5×5 grid. All the measurements were conducted at room temperature, the vertical indentation rate was 5 μm s^{-1} and the sampling frequency was 1 kHz. The adhesion force was determined by the lowest point of the retraction curve. The interfacial stiffness was determined by fitting the slope of the repulsive part of the approach curve. The rupture distance was calculated as the difference between the pull-off displacement and the

snap-in displacement.

PDF analysis. 1 mL of DI water was added onto the PVAAc coat (~5×10^{-2} mg mm^{-2}) on a square glass plate (12×12 mm^2 in area and 2 mm in thickness) followed by letting it stand still at room temperature for 15 min. When the dry PVAAc film fully swelled into the hydrogel coat, the free water was carefully removed by filter paper to prepare the free-swelling hydrogel coating. To obtain the compressive-state hydrogel counterpart, another piece of glass plate was covered on the free-swelling hydrogel coating, followed by applying a compressive load of 21.6 N on a Mecmesin multitest 1-i tensile and compression test system. The transudatory water was removed by filter paper during 10 min-retained compressive loading. X-ray diffraction data of the two-state hydrogel coatings supported by glass substrate was collected on a Bruker D8 ADVANCE at Cu Kα radiation (λ = 1.54056 Å) with the two-theta degree range from 5° to 145° at a scanning rate of 2° min^{-1}. The used X-ray tube voltage and current were 40 kV and 40 mA, respectively. The pair distribution function was directly calculated from the measured total scattering function through Fourier transformation by using PDFgetX3[35].

Fractal and multifractal analysis. The Minkowski-Bouligand dimension D of a fractal topological structure was determined through a classic box-counting method, according to the following equation[36]:

$$\boldsymbol{D} = \lim_{\varepsilon\to 0}\frac{\log \boldsymbol{N}(\varepsilon)}{\log\frac{1}{\varepsilon}}$$

where $N(\varepsilon)$ is the number of boxes of side length ε required to cover the geometric structure. D is estimated as the exponent of a power law representing the fractal dimension of a certain structure. Moreover, the multifractal spectrum, also known as the singularity spectrum, namely the relationship between the Hausdorff dimension f and the average singularity strength α, was used to identify heterogeneity of kinetic process and quantify structural complexity, which was determined through previously-reported method according to the following implicit functions of the distorting exponent q[37]:

$$\alpha(\boldsymbol{q}) = \lim_{\varepsilon\to 0}\frac{\sum_{i=1}^{N}\frac{[\boldsymbol{P}_i(\varepsilon)]^q}{\sum_{j=1}^{N}[\boldsymbol{P}_i(\varepsilon)]^q}\log[\boldsymbol{P}_i(\varepsilon)]}{\log\varepsilon}$$

$$\boldsymbol{f}(\boldsymbol{q}) = \lim_{\varepsilon\to 0}\frac{\sum_{i=1}^{N}\frac{[\boldsymbol{P}_i(\varepsilon)]^q}{\sum_{j=1}^{N}[\boldsymbol{P}_i(\varepsilon)]^q}\log\{\frac{[\boldsymbol{P}_i(\varepsilon)]^q}{\sum_{j=1}^{N}[\boldsymbol{P}_i(\varepsilon)]^q}\}}{\log\varepsilon}$$

where $P_i(\varepsilon)$ is the probability (integrated measure) in the ith box of longitude ε, namely a fraction of the amount of pixels in each box. The multifractal analyses were performed to both of the (quasi)-bicontinuous solid network and the corresponding gaseous network, which were extracted from a typical SEM picture in advance through ImageJ.

In-situ observation of the membrane growth. The growth processes of AgCl, $BiVO_4$ and Ag_2CrO_4 membranes on aqueous surface were recorded by using an H1600 industrial camera through the S-EYE

software. The experiments were performed in a windshield box on a vibration isolator. The temperature was controlled by a bottom electronic heating plate. The reaction temperature was 35, 50, 55 °C for AgCl, $BiVO_4$ and Ag_2CrO_4 membrane synthesis, respectively. A ring LED was employed in reflection mode as the lighting source. The vertical focal length was fixed in advance through focusing on the aqueous surface of 3 mL DI water held in a pretreated Petri dish. After igniting the reaction by a quick addition of all the reactant solution, the kinematic evolution of the floating solids on the aqueous surface was simultaneously recoded at a frame rate of 30 fps with the resolution of 1920×1080. All the video editing were performed in Shotcut. Based on the particle imaging velocimetry (PIV) algorithm, the velocity field was calculated by performing correlation analysis on the positions of the floating particles between successive video frames using the PIVlab written in Matlab[38].

Data availability

The data that support the findings of this study are available from the corresponding author on reasonable request.

Code availability

The customized procedures used to solve kinematic equation, calculate collision energy and perform dynamic GT phase simulation is provided in Supplementary Information (Section S8.).

Acknowledgements

This research is supported by A*STAR under its 2019 AME IRG & YIRG Grant Calls, A2083c0059 as well as NRF Central Gap Fund NRF2020NRF-CG001-023 and NUS TAP25002021-01-01.

Author contributions

C.Z. and G.W.H. conceived the idea. C.Z. designed and performed most of the experiments and theoretical derivations. Y.X. assisted in some membrane characterizations as well as video editing. W.L and K.Z. supported the AFM experiments. G.W.H. supervised the project. C.Z. and G.W.H. analysed all the data and wrote the manuscript. All authors commented on the manuscript.

Competing interests

The authors declare no competing interests.

References

1 Kotyk, A. Membranes as the mediators of flow of matter, energy and information. *Polym. J.* **23**, 629-639 (1991).

2 Cieśla, A. Theoretical consideration for oxygen enrichment from air using high-T_C superconducting membrane. *PRZEGLĄD ELEKTROTECHNICZNY* **88**, 40-43 (2012).

3 Alvarez, P. J., Chan, C. K., Elimelech, M., Halas, N. J. & Villagrán, D. Emerging opportunities for nanotechnology to enhance water security. *Nat. Nanotechnol.* **13**, 634-641 (2018).

4 Lee, K. C. The Fabrication of Thin, Freestanding, Single-Crystal, Semiconductor Membranes. *J. Electrochem. Soc.* **137**, 2556 (1990).

5 Lu, D. *et al.* Synthesis of freestanding single-crystal perovskite films and heterostructures by etching of sacrificial water-soluble layers. *Nat. Mater.* **15**, 1255 (2016).

6 Dong, G. *et al.* Super-elastic ferroelectric single-crystal membrane with continuous electric dipole

582 rotation. *Science* **366**, 475-479 (2019).
583 7 Genet, C. & Ebbesen, T. W. Light in tiny holes. *Nature* **445**, 39-46 (2007).
584 8 Shi, Y., Bork, A. H., Schweiger, S. & Rupp, J. L. M. The effect of mechanical twisting on oxygen ionic
585 transport in solid-state energy conversion membranes. *Nat. Mater.* **14**, 721-727 (2015).
586 9 Nair, J. P., Wachtel, E., Lubomirsky, I., Fleig, J. & Maier, J. Anomalous expansion of CeO_2
587 nanocrystalline membranes. *Adv. Mater.* **15**, 2077-2081 (2003).
588 10 Liu, Z. *et al.* Crosslinking ionic oligomers as conformable precursors to calcium carbonate. *Nature* **574**,
589 394-398 (2019).
590 11 Lalia, B. S., Kochkodan, V., Hashaikeh, R. & Hilal, N. A review on membrane fabrication: Structure,
591 properties and performance relationship. *Desalination* **326**, 77-95 (2013).
592 12 Lu, X. & Elimelech, M. Fabrication of desalination membranes by interfacial polymerization: History,
593 current efforts, and future directions. *Chem. Soc. Rev.* **50**, 6290-6307 (2021).
594 13 Tan, Z., Chen, S., Peng, X., Zhang, L. & Gao, C. Polyamide membranes with nanoscale Turing structures
595 for water purification. *Science* **360**, 518-521 (2018).
596 14 Wang, Z. *et al.* On-water surface synthesis of charged two-dimensional polymer single crystals via the
597 irreversible Katritzky reaction. *Nat. Synth.* **1**, 69-76 (2022).
598 15 Ou, Z. *et al.* Oriented Growth of Thin Films of Covalent Organic Frameworks with Large Single-
599 Crystalline Domains on the Water Surface. *J. Am. Chem. Soc.* (2022).
600 16 Haviland, D. B. Quantitative force microscopy from a dynamic point of view. *Curr. Opin. Colloid*
601 *Interface Sci.* **27**, 74-81 (2017).
602 17 Yang, C. & Suo, Z. Hydrogel ionotronics. *Nat. Rev. Mater.* **3**, 125-142 (2018).
603 18 Gopinath, A. & Mahadevan, L. Elastohydrodynamics of wet bristles, carpets and brushes. *P. Roy. Soc.*
604 *A-Math. Phy.* **467**, 1665-1685 (2011).
605 19 Kemp, M. Silver mirror. *J. Chem. Educ.* **58**, 655 (1981).
606 20 Zhu, Y. *et al.* Size effects on elasticity, yielding, and fracture of silver nanowires: In situ experiments.
607 *Phys. Rev. B* **85**, 045443 (2012).
608 21 Mogensen, K. B. & Kneipp, K. Size-dependent shifts of plasmon resonance in silver nanoparticle films
609 using controlled dissolution: monitoring the onset of surface screening effects. *J. Phys. Chem. C* **118**,
610 28075-28083 (2014).
611 22 Uhlenbeck, G. E. & Ornstein, L. S. On the theory of the Brownian motion. *Phys. Rev.* **36**, 823 (1930).
612 23 Vella, D. & Mahadevan, L. The "cheerios effect". *Am. J. Phys.* **73**, 817-825 (2005).
613 24 Dixit, H. N. & Homsy, G. Capillary effects on floating cylindrical particles. *Phys. Fluids* **24**, 122102
614 (2012).
615 25 Bai, X.-M. *et al.* Role of atomic structure on grain boundary-defect interactions in Cu. *Phys. Rev. B* **85**,
616 214103 (2012).
617 26 Hwang, S., Nishimura, C. & McCormick, P. Mechanical milling of magnesium powder. *Mater. Sci. Eng.*
618 *A* **318**, 22-33 (2001).
619 27 Jiang, W. *et al.* Emergence of complexity in hierarchically organized chiral particles. *Science* **368**, 642-
620 648 (2020).
621 28 García-Domenech, R., Gálvez, J., de Julián-Ortiz, J. V. & Pogliani, L. Some new trends in chemical graph
622 theory. *Chem. Rev.* **108**, 1127-1169 (2008).
623 29 Packard, N. H. & Wolfram, S. Two-dimensional cellular automata. *J. Stat. Phys.* **38**, 901-946 (1985).
624 30 Wolfram, S. Cellular automata as models of complexity. *Nature* **311**, 419-424 (1984).
625 31 Wan, K.-T., Guo, S. & Dillard, D. A. A theoretical and numerical study of a thin clamped circular film

under an external load in the presence of a tensile residual stress. *Thin Solid Films* **425**, 150-162 (2003).
32 Komaragiri, U., Begley, M. & Simmonds, J. The mechanical response of freestanding circular elastic films under point and pressure loads. *J. Appl. Mech.* **72**, 203-212 (2005).
33 Lee, C., Wei, X., Kysar, J. W. & Hone, J. Measurement of the elastic properties and intrinsic strength of monolayer graphene. *Science* **321**, 385-388 (2008).
34 Cuenot, S., Frétigny, C., Demoustier-Champagne, S. & Nysten, B. Surface tension effect on the mechanical properties of nanomaterials measured by atomic force microscopy. *Phys. Rev. B* **69**, 165410 (2004).
35 Juhás, P., Davis, T., Farrow, C. L. & Billinge, S. J. PDFgetX3: a rapid and highly automatable program for processing powder diffraction data into total scattering pair distribution functions. *J. Appl. Crystallogr.* **46**, 560-566 (2013).
36 Liebovitch, L. S. & Toth, T. A fast algorithm to determine fractal dimensions by box counting. *Phy. Lett. A* **141**, 386-390 (1989).
37 Chhabra, A. & Jensen, R. V. Direct determination of the f (α) singularity spectrum. *Physical Review Lett.* **62**, 1327 (1989).
38 Thielicke, W. & Stamhuis, E. PIVlab-towards user-friendly, affordable and accurate digital particle image velocimetry in MATLAB. *J. Open Res. Softw.* **2** (2014).

Supplementary Files

This is a list of supplementary files associated with this preprint. Click to download.

- SupplementaryVideo1.mp4
- SupplementaryVideo5.mp4
- SupplementaryVideo4.mp4
- SupplementaryInformation.pdf
- SupplementaryVideo2.mp4
- SupplementaryVideo3.mp4
- ExtendedData.pdf